https://doi.org/10.5194/egusphere-2026-531
Preprint. Discussion started: 2 April 2026

Aerosol-cloud interactions in Saharan mineral dust over the Eastern Mediterranean

Maximilian Dollner[1], Josef Gasteiger[1, a], Konrad Kandler[2], Manuel Schöberl[1], Sudharaj Aryasree[2], Benjamin Witschas[3] and Bernadett Weinzierl[1]

[1] University of Vienna, Faculty of Physics, Aerosol Physics and Environmental Physics, Vienna, Austria
[2] Institute of Applied Geosciences, Technical University of Darmstadt, Darmstadt, Germany
[3] Institut für Physik der Atmosphäre, Deutsches Zentrum für Luft- und Raumfahrt (DLR), Oberpfaffenhofen, Germany
[a] Now at: Hamtec Consulting GmbH at EUMETSAT, Darmstadt, Germany

Correspondence to: maximilian.dollner@univie.ac.at; bernadett.weinzierl@univie.ac.at

Abstract. Mineral dust is a major component of atmospheric aerosol mass, yet its role in cloud processes remains poorly understood. While laboratory studies have explored its ability to act as cloud condensation nuclei (CCN) and ice nucleating particles (INPs), in situ atmospheric measurements are scarce.

This study presents unique in situ and remote sensing observations of dust-embedded clouds from the A-LIFE campaign in the Eastern Mediterranean. Aircraft observations on 20 April 2017 including shadow images and size distributions of aerosol and cloud particles combined with Doppler wind lidar (DWL) measurements were used to characterize dust and cloud microphysical properties. A novel size distribution retrieval for the second-generation Cloud, Aerosol, and Precipitation Spectrometer (CAPS) was developed – accounting for instrumental uncertainties, particle non-sphericity, and refractive index via a Monte Carlo method – and a machine learning-based calibration of the CAPS hotwire sensor for LWC measurements was introduced.

Using the newly developed analysis tools, this study presents a quantitative assessment of two different aerosol-cloud interaction processes in dust-embedded clouds: Measurements at the cloud-top indicated heterogeneous ice nucleation, in accordance with laboratory experiments and INP parameterizations. Furthermore, small-scale CCN activation of mineral dust particles into liquid droplets (~10 µm) was observed in the middle part of the cloud, with activation diameters as small as 0.13–0.23 µm, consistent with laboratory findings. DWL observations revealed vertical lifting as the driver of increased water supersaturation, enabling CCN activation. These findings provide new insights into the microphysical processes of dust-embedded clouds and their interactions with the atmosphere.

https://doi.org/10.5194/egusphere-2026-531
Preprint. Discussion started: 2 April 2026

1 Introduction

Although approx. 70% of the atmospheric aerosol mass consists of mineral dust (Huneeus et al., 2011; Kinne et al., 2006), it remains a significant contributor to the uncertainties of predictions of the Earth's energy budget (Adebiyi and Kok, 2020). The direct impact of mineral dust on the atmospheric energy budget depends on the size of the particles. Fine dust has a predominantly cooling effect by scattering shortwave solar radiation, whereas coarse dust warms the atmosphere by absorbing solar and terrestrial radiation (Kok et al., 2017). Several studies have shown that the removal rates of larger super-micron dust particles are slower than expected (e.g. Adebiyi et al., 2023; Mateos et al., 2026; Ratcliffe et al., 2024; Ryder et al., 2019; Weinzierl et al., 2009, 2011, 2017). Global climate models tend to underestimate the amount of coarse-mode mineral dust particles. This misrepresentation overestimates the cooling effect by 0.15 W m^{-2} (0.1 to 0.24 W m^{-2}) and increases the likelihood of a general warming effect of mineral dust (Adebiyi and Kok, 2020).

Besides the direct interaction with radiation, mineral dust also affects the Earth's atmosphere with its ability to act as cloud condensation nuclei (CCN) and ice nucleating particles (INPs). CCNs are aerosol particles that activate and grow to liquid cloud droplets within a water vapor supersaturated environment (Seinfeld and Pandis, 2006). The CCN ability of a particular aerosol particle depends on its size and chemical composition. A widely used parameterization of this dependency is the κ-Köhler theory, which uses the parameter κ to describe this relative humidity-dependent growth of aerosol particles for different compositions and particle sizes (Petters and Kreidenweis, 2007). The CCN activity of mineral dust has been investigated by several laboratory studies. Tang et al. (2016) provide a comprehensive literature review of these studies, revealing a good agreement throughout the different laboratory observations. Single component mineral dust (e.g., illite, kaolinite, montmorillonite) appears to have a very low CCN activity, which can be described with κ<0.01. However, authentic samples of North African, Saharan, and Asian dust are reported with slightly higher κ in the range between 0.01 and 0.023.

INPs are the fundamental component of heterogeneous ice nucleation, which is the mechanism of primary ice formation at temperatures larger than 235 K. There are different modes of heterogeneous ice nucleation and definitions have been subject to change in the past (Kanji et al., 2017). Vali et al. (2015) describe the heterogeneous ice nucleation modes as follows: Deposition nucleation is the growth via direct deposition of supersaturated vapor on an INP, whereas freezing nucleation includes a liquid state. Freezing nucleation can be separated into immersion freezing, contact freezing, and condensation freezing. For immersion and contact freezing, the ice nucleation is initiated by an INP, with the difference that the INP is immersed within the liquid droplet for immersion freezing. Condensation freezing is defined as the concurrent initiation of the liquid droplet formation process and the freezing process, where the droplet formation happens at conditions below the melting point of ice.

Numerous laboratory studies investigated the ice nucleation ability of mineral dust. Kanji and Abbatt (2006) investigated the deposition mode nucleation of mineral dust in the temperature range between 218 and 263 K. For a Saharan dust sample with particle sizes ranging from 0.5 to 5 µm, they found an ice onset relative humidity with respect to ice (RH_i) between 102 and 108% with no strong dependency on temperature. Findings from Kanji and Abbatt (2006) were confirmed by other studies of ice nucleation of super-micron dust (Hoose and Möhler, 2012). However, current global-climate models underestimate the effect of dust aerosol on cloud formation. A model-tuning study used the hemispheric and seasonal contrast of cloud top phase from satellite observations to constrain the dust-driven droplet freezing in a global-climate model (Villanueva et al., 2021). They revealed an effect of 0.14 ± 0.13 W m^{-2} due to dust-based immersion freezing of droplets between 30°N and 60°N.

https://doi.org/10.5194/egusphere-2026-531
Preprint. Discussion started: 2 April 2026

In our study, airborne in situ observations are used to improve the understanding of atmospheric CCNs and INPs. However, atmospheric in situ measurements of CCN activation and ice nucleation events are challenging because the timing and location of the microphysical process are difficult to predict.

A method to measure the ice nucleation ability of aerosol particles directly in the atmosphere was conducted during recent airborne in situ investigations (Cziczo et al., 2017). Residuals of evaporated ice crystals (i.e., particles remaining after the evaporation of the ice crystal) revealed information about the chemical composition and size of the aerosol particles that initiated the ice crystal formation. The analysis of the residuals can be done either offline using optical and other microscopy techniques (see also section c of Cziczo et al., 2017) or online with instruments like a real-time mass spectrometer (e.g., Eidhammer et al., 2010). A study using such an online method found mineral dust and metallic particles as the dominant INP of the measured ice crystals (Cziczo et al., 2013). Induced nucleation of ambient aerosol in a portable chamber of controlled temperature and saturation is another in situ method to investigate the cloud condensation and ice nucleation properties of the ambient aerosol. In situ measurements are often combined with model simulations and satellite observations to gain knowledge about the nucleation process and responsible INPs (e.g. Jensen et al., 2018). Such a combined approach of global-scale airborne in situ measurements of dust aerosol in the upper troposphere and detailed cirrus-formation simulations determined the dominant role of dust aerosol in the cirrus formation process in the northern hemispherical extra-tropics in all seasons (Froyd et al., 2022). However, such atmospheric in situ observations are rare and additional investigations are necessary to reduce knowledge gaps connected to atmospheric CCN and INP processes.

Based on data from the A-LIFE field experiment in the Mediterranean (Weinzierl and Coauthors, in prep.) this study presents a quantitative assessment of two distinct aerosol-cloud interaction processes in clouds embedded in a Saharan mineral dust layer. Airborne in situ measurements of mineral dust, pollution, and clouds were conducted with the German Aerospace Center (DLR) Falcon 20 E-5, equipped with an extensive aerosol and cloud payload and a Doppler wind lidar (DWL). On 20 April 2017, in situ measurements within a mineral dust layer and clouds revealed two distinct processes of aerosol-cloud interactions in the dust-embedded clouds. In this study, we first examine the hypothesis that heterogeneous ice nucleation of super-micron mineral dust particles formed the ice crystals at the top of a cloud. Second, we provide a detailed analysis of the unique capture of small-scale activation and growth of mineral dust particles to liquid droplets within the embedded cloud.

https://doi.org/10.5194/egusphere-2026-531
Preprint. Discussion started: 2 April 2026

2 Method

This chapter introduces the methods relevant for analyzing the aerosol-cloud interactions in the mineral dust layer. The chapter is structured as follows: section 2.1 describes the A-LIFE field experiment, and section 2.2 follows with an introduction of the second-generation Cloud, Aerosol, and Precipitation Spectrometer (CAPS) and its associated data analysis algorithms. The presented algorithms include the *Cloud Indicator* for cloud detection and classification, a novel size distribution retrieval, and a newly developed calibration method for the CAPS hotwire sensor for LWC. This chapter ends with information on the offline chemical analysis of particles collected from the mineral dust layer and the introduction of the DWL in sections 2.3 and 2.4, respectively.

2.1 A-LIFE field campaign

The "Absorbing aerosol layers in a changing climate: aging, lifetime and dynamics (A-LIFE)" project was funded by the European Research Council (ERC) to investigate the properties of mixtures of absorbing aerosols in the Eastern Mediterranean (Groß et al., 2025; Schöberl et al., 2024; Teri et al., 2025; Weinzierl and Coauthors, in prep.). Furthermore, properties and lifetime of coarse-mode aerosol particles and the processes allowing these large particles to remain lofted were particularly interesting for the project. The A-LIFE project deployed the German Aerospace Center (DLR) Falcon 20 E-5 aircraft, which performed research flights from Cyprus between 3 and 30 April 2017. The aircraft was equipped with an extensive aerosol and cloud payload, instruments for meteorological parameters, and a Doppler Wind Lidar (DWL). In total 22 flights with 74h of airborne sampling were conducted, including measurements of multiple dust outbreaks from the Saharan and Arabian deserts, pollution layers, and mixtures of pollution and dust. Cloud observations were focused primarily on the dust-cloud interactions. The airborne in situ observations were assisted and extended by simulations from the Lagrangian transport and dispersion model FLEXPART (Pisso et al., 2019; Seibert and Frank, 2004; Stohl et al., 1998, 2005; Tipka et al., 2020).

2.2 Second-generation Cloud, Aerosol, and Precipitation Spectrometer

The second-generation Cloud, Aerosol, and Precipitation Spectrometer (CAPS, Droplet Measurement Technologies, Longmont, CO, USA) is a wing-mounted optical spectrometer and optical array probe for measurements of aerosol and cloud particles in the nominal size range between 0.5 and 930 µm. The CAPS measurements provided input for two algorithms used in this study. First, the *Cloud Indicator* algorithm (Dollner et al., 2024) was used to separate periods inside clouds from cloud-free sequences. Furthermore, a novel algorithm – summarized in this study – was developed to calculate particle size distributions accounting for instrumental uncertainties and reporting the particle sizes in geometric diameters. Section 2.2.1 describes the components of the CAPS instrument and gives a brief overview of the standard data products. The *Cloud Indicator* algorithm, the size distribution retrieval, and the hotwire calibration method are specified in chapters 2.2.2, 2.2.3, and 2.2.4, respectively.

2.2.1 Instrument description

The CAPS has two main components: The Cloud and Aerosol Spectrometer (CAS) and the Cloud Image Probe (CIP) (Baumgardner et al., 2001). Additionally, CAPS supplies measurements of true airspeed, pressure, relative humidity, temperature, and liquid water content with supporting sensors. The CAPS from the University of Vienna

https://doi.org/10.5194/egusphere-2026-531
Preprint. Discussion started: 2 April 2026

(UNIVIE-CAPS) is the main instrument used for this study. A detailed description of the UNIVIE-CAPS and the procedure used to calibrate the instrument can be found in Dollner et al. (2024).

CAS is an optical spectrometer that determines the size of aerosol and cloud particles based on the principle of light scattering of single particles intersecting with a laser beam (λ = 658 nm). It measures the scattered light in the forward direction (4.2° – 13.2° for the UNIVIE-CAPS) and covers a size range between approximately 0.5 and 50 µm. Additional detectors also measure backscattered light.

The Cloud Image Probe (CIP) is an optical array probe (OAP) (Knollenberg, 1970) that extends the size range to larger particles. It covers the nominal size range between 15 and 930 µm of aerosol and cloud particles passing a 658 nm collimated laser beam and records shadow images with a linear array of 64 photodiodes with 15 µm resolution. The CIP of the UNIVIE-CAPS is a greyscale version reporting images of measured particles with three intensity levels (setting for A-LIFE: 30%, 50% 70% greyscale).

2.2.2 The Cloud Indicator algorithm

The *Cloud Indicator* is an algorithm that automatically detects and classifies measurement periods inside clouds (Dollner et al., 2024). The algorithm utilizes size distribution, relative humidity, and temperature measurements to distinguish periods in cloud-free, Aerosol-Cloud Transition Regime (ACTR), liquid clouds, clouds in the Mixed-Phase Temperature Regime (MPTR), and cirrus clouds. An additional cloud-aerosol volume factor (f_{ca}) is used to ensure a robust distinction of aerosol layers with an enhanced coarse-mode concentration (e.g., a mineral dust layer) from clouds and, hence, reduces misclassification of the two. In general, the input data to the *Cloud Indicator* algorithm is not restricted to any specific particle sizing instrument; however, for a reliable functionality of the f_{ca} the size distribution input to the *Cloud Indicator* algorithm should cover the range between approx. 0.5 µm and at least 50 µm. For this study, size distribution measurements were taken from the UNIVIE-CAPS.

2.2.3 UNIVIE size distribution retrieval

Particle size distributions are commonly reported with equivalent optical diameters (e.g., spherical ammonium sulfate equivalent), where reported diameters represent the size of a particle of the equivalent material having the same measured signal. The new retrieval used in this study reports particle sizes as geometric diameter and applies a Monte Carlo method (Metropolis and Ulam, 1949) for the consideration of instrumental uncertainties, as well as refractive indices and non-sphericity of the measured aerosol. In optical spectrometers, the scattered light is detected with photodetectors and recorded as a digital signal, where the amplitude of the signal (i.e., scattering signal amplitude) corresponds to the intensity of the scattered light. Calibrations are used to determine the instrument-specific relationship between the scattering signal amplitude and the theoretical scattering cross-section (Szymanski et al., 2009; Walser et al., 2017). The calibration procedure introduced in Dollner et al. (2024) provides this relationship independent of the used calibration material's refractive index and is the foundation for the size distribution retrieval explained in this section.

The main input for the size distribution retrieval consists of scattering signal amplitudes from the CAS particle-by-particle data (PbP-data), information about the type of the measured particles, and the scattering cross-section functions representing the different particle types (e.g. mineral dust, sulfates, organics etc.) and shapes.

Particle classes and CAS scattering cross-section functions

To select the correct scattering cross-section functions for the size distribution retrieval, information about contributing particle types in a measured airmass is necessary. There are several possibilities to retrieve this

https://doi.org/10.5194/egusphere-2026-531
Preprint. Discussion started: 2 April 2026

information as for instance by use of in situ measurements. For example, mass-spectrometers can provide information about the chemical composition of the aerosol particles in an airmass (e.g., Brock et al., 2021). For the A-LIFE data set, the aerosol type was determined using FLEXPART simulations of mass fractions of different chemical components along the flight track. The simulation output was processed to provide time series of number fractions of the contributing aerosol types: mineral dust (dust), sea salt (SS), sulfates (SO4), organics (OM), and black carbon (BC). Additionally, water and ice were added as types for clouds. The seven types build the set of particle classes for the size distribution retrieval as summarized in Table 1. Ensembles of scattering cross-section functions were calculated for each of the seven classes, representing a possible range of refractive indices. Figure 1 visualizes the corresponding scattering cross-section ensembles of all seven classes. SS, SO4, and OM are hygroscopic materials, hence water uptake was also considered for the refractive indices and the particle densities using a volume weighting and the κ-dependent growth factor (Petters and Kreidenweis, 2007; Zieger et al., 2013). Table 1 summarizes the refractive index ranges, the hygroscopicity values κ, and the particle densities (Bond and Bergstrom, 2006; Brock et al., 2021; Froyd et al., 2019; Kandler et al., 2011; Koehler et al., 2009; Michel Flores et al., 2012; Moise et al., 2015; Petters and Kreidenweis, 2007; Svenningsson et al., 2006; Tang, 1996; Zieger et al., 2017) for the corresponding classes as they are used in the UNIVIE size distribution retrieval. For mineral dust, the refractive indices were used from Kandler et al. (2011), which represent composition-dependent refractive indices for different mineral dust components. Scattering cross-section functions for SO4, OM, BC, hydrated SS, and water, are calculated for spherical particles, whereas for dust, dry SS, and ice, non-spherical particles were assumed, and their scattering cross-section ensembles also considered different particle shapes and orientations.

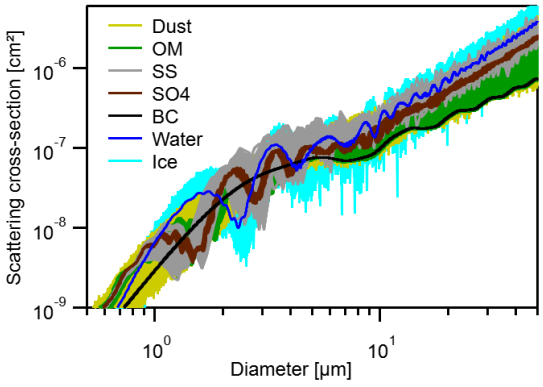

Figure 1. Scattering cross-section ensembles of particle classes for CAS geometry used in the novel UNIVIE size distribution retrieval.

Table 1. Refractive index ranges, κ and density of the different particle classes used in the UNIVIE size distribution retrieval. The ensemble of 'dust' refractive indices is used as explained in Kandler et al. (2011).

Class	Refractive index (λ = 658 nm)		κ	Particle density [kg/m³]
	n	k		
Dust	Kandler et al. (2011)		0.03	2500
SS	1.541	0	1.1	1800
SO4	1.5-1.53	0	0.483	1770
OM	1.44-1.61	0-0.03	0.163	1350
BC	1.75-1.95	0.63– 0.79	0	1000
Water	1.33	0	-	1000
Ice	1.31	0	-	917

https://doi.org/10.5194/egusphere-2026-531
Preprint. Discussion started: 2 April 2026

Binning, "perfect diameter", and "slope correction"

The size distribution retrieval applies the "perfect diameter" method (Rosenberg et al., 2012), which is briefly described here. First, the scattering cross-section values corresponding to the CAS detection range are divided into discrete bins to generate a binning. As the scattering cross-section functions for the geometry of the CAS optics yields a non-monotonic relationship between particle diameter and the CAS scattering cross section (see Figure 1), the mapping from instrument-specific scattering cross section to particle diameter is not one-to-one. As a result, one CAS scattering cross section value can be associated with several particle sizes. However, equations 11 and 12 from Rosenberg et al. (2012) calculate bin center diameters and bin widths taking these non-monotonic effects into account. This approach provides bins with representative diameters and bin widths for the CAS-specific scattering response. The method is applied to the scattering cross-section function ensembles of the different classes leading to ensembles of bin center diameters and bin widths for each class.

Depending on the scattering cross-section function, some bins need to be larger to avoid errors from scattering cross-section ambiguities. However, the bin-center diameter depends on the shape of the size distribution. Thus, in regions of the size distribution where the number concentration decreases with increasing diameters (i.e., negative slope of the size distribution), a smaller bin-center diameter should be used to avoid oversizing. Conversely, when the particle number concentration increases with particle diameter (i.e., positive slope of the size distribution), a larger bin center diameter should be used to avoid undersizing. The UNIVIE size-distribution retrieval presented here approximates the bin-center diameter with a sigmoidal function – based on the local slope of the size distribution at each bin – to correct for over- and undersizing.

UNIVIE size distribution retrieval

Figure 2 shows a flowchart of the size distribution retrieval, where the core of the retrieval is within the grey-shaded box. For the size distribution calculations of a selected time period, measurements of scattering signal amplitudes are taken from the corresponding PbP data and converted to scattering cross-sections using a calibration valid for the measurement period (Dollner et al., 2024). The retrieved scattering cross-section values are sorted into the scattering cross-section bins of the specific particle class, which returns a count distribution for the selected time period. The count distribution is converted into particle size distributions (i.e., dN/dlogD in cm^{-3}) at STP conditions[1] using the following equations:

$$\overline{N_i} = \frac{\sum_j^n \frac{N_{i,j} * (f_{PbP})_j * (f_{STP})_j}{\Delta t_j * TAS_j * SA}}{n} \quad \textbf{(1)}$$

$$\frac{dN}{dlogD} = \frac{\overline{N_i} * \varepsilon}{w_i} * \ln(10) * D_i \quad \textbf{(2)}$$

Here, $N_{i,j}$ represents the counts of the i-th bin for a specific data point j, $\overline{N_i}$ is the average bin concentration for the selected time period, n is the number of used data points in the time period. For a specific data point j, $(f_{STP})_j$ is the PbP-factor[2], Δt_j is the sampling time in seconds, and TAS_j the true airspeed in cm s^{-1}. SA the sample area of the CAS in cm^2. For equation (2), ε represents a systematic error that covers uncertainties of TAS, temperature, and pressure measurements. D_i and w_i are the bin-center diameters and bin widths, respectively, using the "perfect diameter" method as described above. The resulting particle size distributions are corrected for the slope-

[1] STP: corrected to conditions at standard pressure (1013.25 hPa) and standard temperature (273.15 K)
[2] PbP recordings are limited to a certain number of particles. If the number concentration is larger than this limit a scaling factor is applied.

https://doi.org/10.5194/egusphere-2026-531
Preprint. Discussion started: 2 April 2026

dependent over- and under-sizing. Furthermore, a sampling efficiency correction of flow-induced undercounting of small particles is applied (Spanu et al., 2020). Measurements of CAPS are at near ambient conditions; hence, the calculated particle size distributions represent the aerosol at ambient relative humidity. The retrieval applies a numerical solution of the κ -Köhler theory to also obtain the particle size distribution at dry relative humidity conditions (Brock et al., 2016).

The presented process is part of a Monte Carlo simulation and is repeated numerous times (the number of repetitions depends on computing power of the setup - a good range is between 200 and 1000 repetitions). For each repetition, the following input values are randomly selected:

- Scattering signal amplitudes from the CAS PbP data of the selected time period
- Calibration coefficients generated from the reported calibration uncertainties
- Bincenter diameter (D_i) and bin width (w_i) from an ensemble for the corresponding particle class
- Systematic errors (ε) of up to 20%, covering uncertainties of TAS, temperature, and pressure measurements

The output of the Monte Carlo simulation is an ensemble of particle number size distributions for one particle class, e.g. mineral dust. Calculations for all classes, which have contributing particles in the airmass of the selected period, constitute a set of size distribution ensembles.

Since the binning of the different classes is unequal, a linear interpolation on a lognormal diameter grid is applied for the size distribution ensembles of all classes, followed by the combination of the size distribution ensembles of the different classes based on their proportional contribution to the observed air mass. The final outputs of the retrieval are two ensembles of size distributions, one for dry and one for ambient relative humidity conditions, reflecting instrumental uncertainties and covering the range of geometric sizes of the measured particle composition. In summary, this approach enables a more reliable and precise measurement and quantification of atmospheric coarse-mode aerosol and cloud particles detected with an optical particle counter.

https://doi.org/10.5194/egusphere-2026-531
Preprint. Discussion started: 2 April 2026

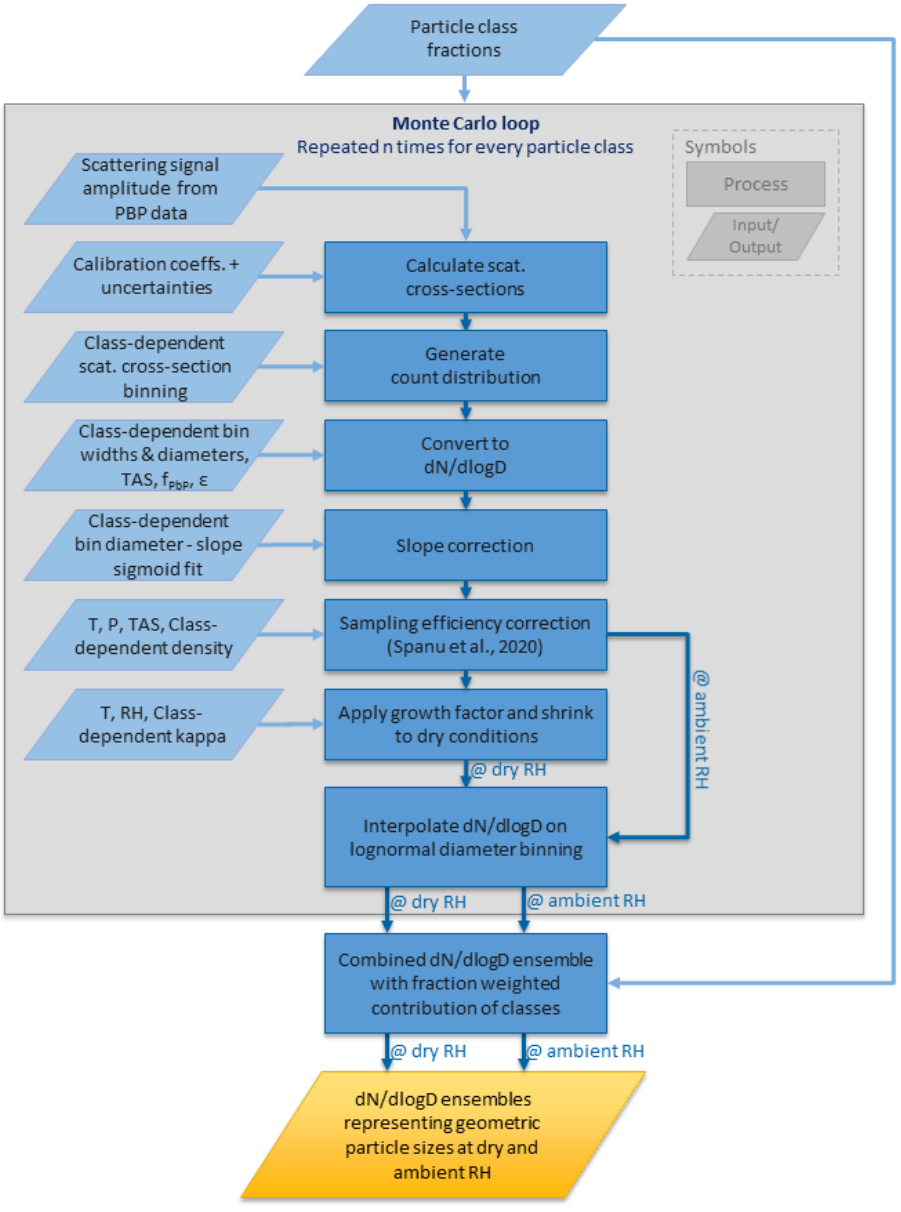

Figure 2. Flowchart of the novel UNIVIE size distribution retrieval. Rectangles represent processes and rhomboids inputs and outputs of the retrieval, where the golden rhomboid indicates the final dN/dlogD output. The part inside the grey box is calculated for all particle classes separately and represents the Monte Carlo loop of the retrieval. ε represents a systematic uncertainty and f_{PbP} is the PbP-factor. For further details, see text.

https://doi.org/10.5194/egusphere-2026-531
Preprint. Discussion started: 2 April 2026

2.2.4 Novel machine learning method for hotwire calibration

The liquid water content sensor used in the CAPS instruments is a King probe hotwire sensor (King et al., 1978). Baumgardner et al. (2017) describe the measurement principle as the energy, in the form of an electrical current, required to keep a cylindrical wire (called the hotwire) at a constant temperature. At the hotwire, energy is lost due to radiation, convection, and evaporation of droplets. The radiation component has only a minor contribution and is neglected for the calculations, which leaves convection and evaporation as the only two major energy sinks. After the subtraction of the convection term from the measured energy consumption, the remaining contribution results from the evaporation of liquid water at the hotwire. The remaining energy consumption due to evaporation can be used to calculate the LWC of the measured liquid droplets.

Generally, there are two ways to estimate the convection term: a) averaging the power consumption measured before and after a targeted cloud, or b) using the airspeed and air density at the location of measurement. The optimum parameterization method (OPM) presented in McFarquhar et al. (2017) provides a method to iteratively approximate parameters for calculating the convection term. For the OPM method, measurements outside of clouds, where only the convection determines the measured energy consumption, are used to optimize the parameters by reducing the error between calculated and measured convection. The Machine Learning (ML) method introduced in this study is partly comparable to the OPM method since it also utilizes the measured power outside of clouds. However, instead of iteratively optimizing parameters, we utilize a neural network to determine the convection component only using three input parameters: the temperature, pressure, and airspeed at the probe location as explained by Spanu et al. (2020). Using the measured power outside of clouds, the neural network trains a model to predict the convection component based on these three input parameters. This trained model is then applied to predict the convective loss for measurements inside clouds. A subtraction of the predicted convective loss from the measured power leaves the evaporation due to the liquid droplets. According to King et al. (1978), measurements with a hotwire LWC sensor are attributed with a minimum threshold of 0.05 g m^{-3} and an uncertainty of ±0.05 g m^{-3}. Cober et al. (2001) reported an uncertainty of 15% and a baseline drift of up to 0.02 g m^{-3}. The application of the novel ML method to the A-LIFE measurement flight from this study provides an average baseline of 0.003 ± 0.001 g m^{-3}.

Even though Hotwire LWC sensors are constructed to only measure the water content of liquid droplets, they also respond to the ice crystals with a measurement of 10-20% of the ice mass (Cober et al., 2001; Field et al., 2004; Korolev et al., 2017, 1998). It is important to consider this ice crystal-induced signal when analyzing measurements of sequences where ice crystals may be present, i.e. in mixed-phase or ice clouds.

2.3 Chemical analysis of sample measurements

During the A-LIFE campaign, aerosol chemical composition and single-particle characteristics were studied using impactor samples collected inside the Falcon aircraft behind an inlet with an cut-off diameter between 2.4 µm and 5.8 µm in mineral dust depending on the true airspeed of the Falcon (for details about the Falcon aerosol inlet, see Schöberl et al. (2024)). Particles were collected on pre-treated transmission electron microscope (TEM) grids and analyzed by scanning electron microscopy coupled with energy-dispersive X-ray spectroscopy (SEM-EDX) for their morphology and chemical composition (for example images of particles collected during A-LIFE, see Figure 4 in Teri et al. (2025)). The normalized atomic concentrations of 18 elements and their element ratios were used to classify each particle into various groups and classes. The current classification schemes include 40 particle groups generally observed in various geographical environments which are then classified under seven major

https://doi.org/10.5194/egusphere-2026-531
Preprint. Discussion started: 2 April 2026

classes, including dust, sea salt, sulfate, nitrate, biomass-burning type, C-dominated, and mixtures. Particles that did not fit into these schemes were grouped under 'other' particles. The major set of rules for dust, sulfate and sea-salt used in the current classification can be found in Kandler et al. (2011). Apart from that two new classes were introduced here which include nitrate and biomass burning salt (more details in Aryasree et al. (2024)). For each impactor sample, the relative abundance of every class is calculated as the fraction of the total particles analyzed. The class 'dust' is constituted by silicate-like particles, clay minerals (mainly illite, kaolinite, chlorite), feldspar-like (K, Na, and Ca types), carbonates, and Fe particles as oxides and hydroxides.

For the current study, the sample collected on 20 April 2017 at 15:55 (see Figure 4) was prepared and quality checked, leaving the composition of 172 single particles in the size range of 100 nm to 2.5 µm for the analysis.

2.4 DLR Doppler wind lidar

The heterodyne detection Doppler wind lidar (DWL), installed in the Falcon aircraft for the A-LIFE campaign, emits laser pulses at a 2 µm wavelength and exploits the Doppler shift of the backscattered light from aerosol and cloud particles to obtain information about atmospheric wind (Witschas et al., 2017). The DLR DWL can operate in two modes: conical scanning, which enables the calculation of the three-dimensional wind with a horizontal resolution of about 8 km, and nadir-pointing mode (Witschas et al., 2017), which offers precise information about the vertical wind with a higher horizontal resolution of about 200 m, but no information about the horizontal wind (Chouza et al., 2016; Witschas et al., 2023). The vertical resolution for both wind products is 100 m. In addition, the DLR DWL further provides insights into aerosol layering and cloud features. While measurements from the DLR DWL can be used to calculate calibrated aerosol backscatter (Chouza et al., 2015, 2017), the uncalibrated backscatter signal can be used as a surrogate for the location of aerosol layers and clouds. For this study, DLR DWL measurements of the vertical wind and uncalibrated backscatter are used.

3 Results

In this section, the methods introduced in section 2 are applied to the A-LIFE measurements performed on 20 April 2017 to assess the formation process for the ice crystals in the cloud-top of the dust-embedded clouds. Furthermore, small-scale CCN activation events, where mineral dust activation and growth led to a large number of small liquid droplets, are studied.

3.1 Introduction of the case study

Particular weather patterns regularly transport mineral dust from African or Arabian deserts to the Mediterranean. The true color-corrected reflectance satellite image from MODIS (Aqua) of Figure 3 visualizes such a mineral dust transport event from the coast of Africa with a northeasterly flow direction on 20 April 2017. The image also shows clouds covering parts of Southern Europe and the Mediterranean Sea. The color-coded line shows the A-LIFE science flight from Heraklion, Crete, to Paphos, Cyprus. The flight extensively sampled a region of the simultaneous presence of a mineral dust layer and clouds embedded into this dust layer on 20 April 2017 south-east of Crete, highlighted with a red rectangle in Figure 3.

https://doi.org/10.5194/egusphere-2026-531
Preprint. Discussion started: 2 April 2026

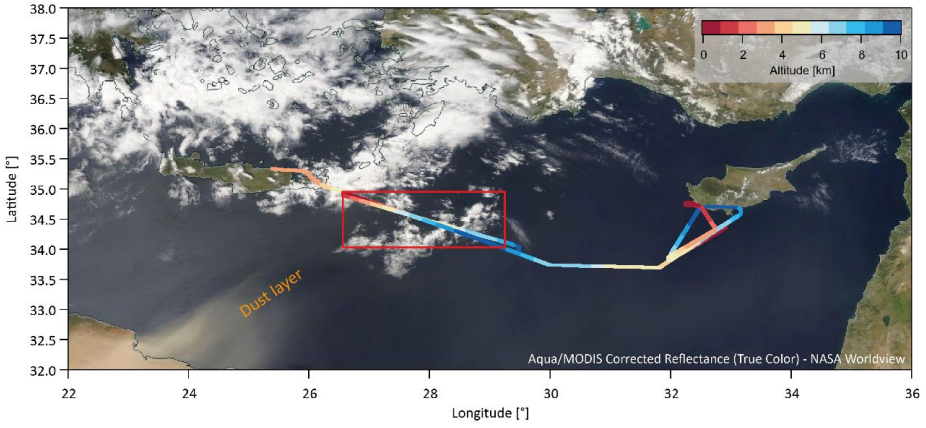

Figure 3. This figure is taken from Dollner et al. (2024). It shows a true color-corrected reflectance satellite image (MODIS; Aqua) of the Mediterranean on 20 April 2017. The satellite image shows mineral dust transported from Africa moving in a northeasterly direction. Clouds predominantly cover the north-western part of the presented region. The altitude-colored line represents the Falcon flight track on 20 April 2017 from Heraklion, Crete, to Paphos, Cyprus. The red frame highlights the region where the mineral dust layer and clouds intersect and represents the region of interest for this study. (NASA Worldview, https://go.nasa.gov/3IjMWG9)

Figure 4 depicts a timeseries of meteorological and cloud-relevant parameters from the red-marked region shown in Figure 3: a) relative humidity with respect to water (dark blue line) and ice (light blue line); b) flight altitude (black line), ambient temperature (red line) and classification of the *Cloud Indicator* with the Aerosol-Cloud Transition Regime (ACTR) shown in yellow, liquid clouds in dark blue, Mixed-Phase Temperature Regime (MPTR) clouds in purple, and cirrus clouds in light blue; c) liquid water content (LWC) measured with the CAPS hotwire sensor (grey dotted line); d) timeseries of the CAPS size distribution with particle diameter on the y-axis and color-coded dN/dlogD concentrations.

The measurement period shown in Figure 4 is characterized by the presence of mineral dust with embedded clouds. According to the three vertical profile measurements conducted in the period between 14:45 and 16:30 (see also Figure 10 for lidar cross-section), the mineral dust layer extends from near the surface to approximately 8 km with a significant number of coarse-mode particles, including particle sizes exceeding 30 µm. During the three vertical profiles between an altitude of 0.6 and 9.1 km, clouds embedded into the dust layer were sampled and classified by the *Cloud Indicator* as Mixed-Phase Temperature Regime (MPTR) clouds with sporadic periods of Aerosol-Cloud Transition Regime (ACTR) (see Figure 4). All three cloud measurements are characterized by elevated relative humidity values, where relative humidity with respect to water (RH_w) and ice (RH_i) mostly exceed 90% and 100%, respectively.

Between 15:53:35 and 15:56:35 at an altitude of 3.2 km, particles were collected for single-particle chemical composition analysis. The composition, presented in Figure 5, is dominated (91%) by mineral dust. The remaining particles consist of NaCl-rich particles, sulfate, nitrate, mixtures and other, with no C-dominated and KCl-rich particles detected. Approximately two-third of the mineral dust particles consist of silicate, the remaining dust particles are composed of kaolinite, carbonate, illite, feldspar, chlorite, or other oxide/hydroxide.

https://doi.org/10.5194/egusphere-2026-531
Preprint. Discussion started: 2 April 2026

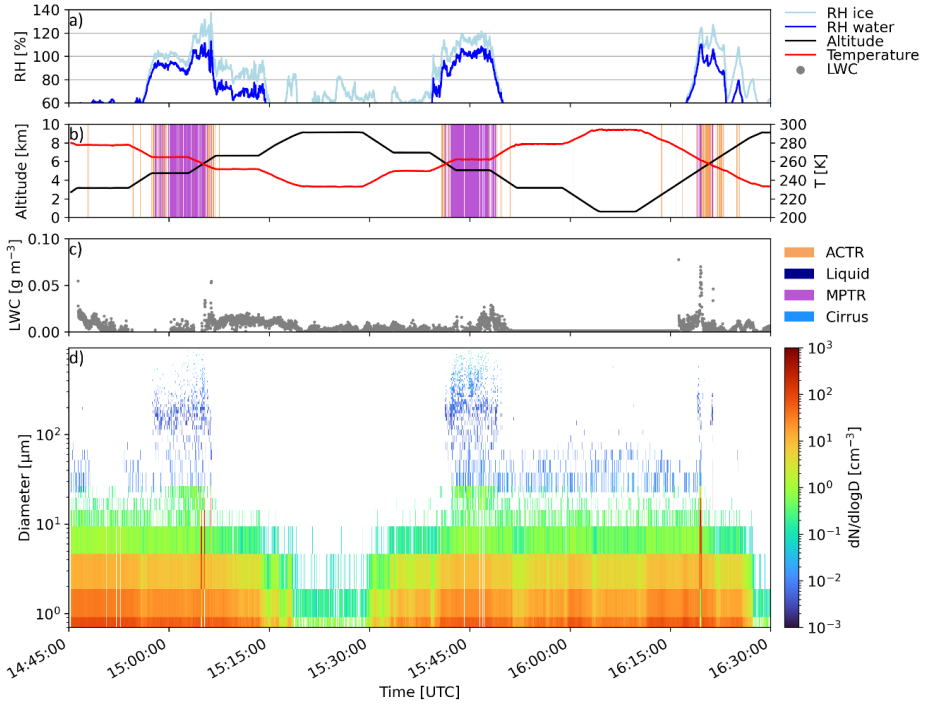

Figure 4. Time series of a) relative humidity with respect to water and ice, b) altitude, temperature, and *Cloud Indicator* classification, c) liquid water content (LWC) measured with the CAPS hotwire sensor, and d) particle size distribution in the size range 0.8 to 25 µm (CAS data) and 25 to 930 µm (CIP data) for the region of interest (red box in Figure 3) of the A-LIFE flight on 20 April 2017.

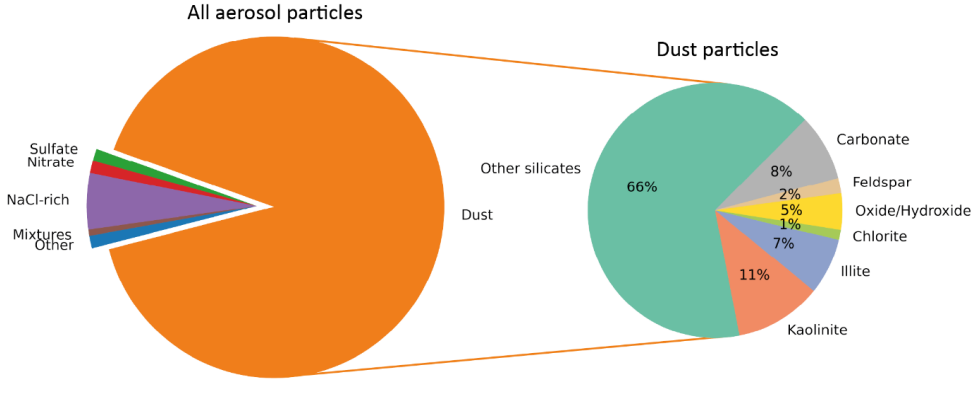

Figure 5. Chemical composition of particles sampled in mineral dust layer outside of clouds between 15:53:35 and 15:56:35 during the flight 20 April 2017.

https://doi.org/10.5194/egusphere-2026-531
Preprint. Discussion started: 2 April 2026

3.2 Investigation of ice crystals in the dust-embedded clouds

Figure 6 presents the vertically-resolved in situ observations of the cloud between 15:40 and 15:49 with panel a) showing the number concentration of particles larger than 30 µm ($N_{D>30\mu m}$) and panel b) displaying the ratio between $N_{D>30\mu m}$ and predicted INPs calculated with the parameterizations for general aerosol according to DeMott et al. (2010) (D10, red dots) and the parameterization for dust aerosol DeMott et al. (2015) (D15, orange dots), both using ambient temperature and number concentration of particles with diameters larger than 500 nm as input. The vertical dashed line in panel b) highlights a ratio of 1 which corresponds to a perfect agreement between predicted INP and measured ice crystal number concentration $N_{D>30\mu m}$. Figure 6c depicts RH_w (blue) and RH_i (light-blue), with the dashed vertical line representing a relative humidity of 100%.

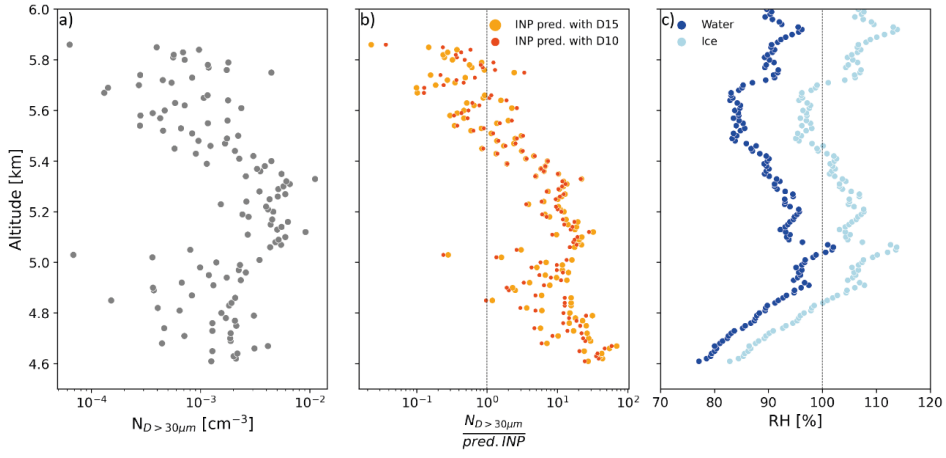

Figure 6. Averaged vertical profiles with 100 m resolution for measurements inside the cloud period between 15:40 and 15:50. Panels show: a) Number concentrations for particles larger than 30µm, b) ratio of number concentration of particles larger than 30µm and predicted INP using parametrization from DeMott et al. (2010) D10 and DeMott et al. (2015) D15, and c) relative humidity with respect to water and ice.

For the lower part of the cloud between 4.6 and 5.0 km, $N_{D>30\mu m}$ is on average 0.002 cm^{-3}, and ratios between $N_{D>30\mu m}$ and the predicted INP number concentrations are mostly above 10. Both RH_w and RH_i are sub-saturated at 4.6 km and increase with increasing altitude. At an altitude of approx. 4.8 km, RH_i reaches 100% and continues to increase up to 106%. Between approx. 5.0 and 5.3 km, the cloud is again supersaturated with respect to ice, and the highest $N_{D>30\mu m}$ of the cloud was observed (average: 0.004 cm^{-3}). From approx. 5.3 to 5.6 km, the airmass is sub-saturated with respect to water and ice, and $N_{D>30\mu m}$ decreases from generally above 10^{-3} cm^{-3} to smaller values. With increasing altitude, $N_{D>30\mu m}$ and the number concentration of predicted INP trend towards equality, as shown with a ratio around 1. Until the top of the cloud at around 5.8 km, $N_{D>30\mu m}$ stays on average below 10^{-3}, whereas the ratio between $N_{D>30\mu m}$ and predicted INP number concentration decreases to values below 1. Above about 5.7 km up to the cloud top, the cloud is again super saturated with respect to ice. Generally, in the upper half of the cloud, ratios calculated with the D10-INP parameterization exceed the ones with D15. In contrast, in the lower half of the cloud, this trend changes, where D15 ratios are larger than D10.

Figure 7 gives insight into the cloud microphysical properties. Measurements inside the cloud are vertically split into seven vertical bins with a resolution of 0.2 km, starting from the cloud base at 4.6 km to the cloud top at 5.8 km. With increasing altitude, the cloud temperature decreases. Average temperatures for the vertical bins are indicated next to the altitude information. Each row of images shows examples of the ice crystals recorded within

https://doi.org/10.5194/egusphere-2026-531
Preprint. Discussion started: 2 April 2026

the corresponding altitude bin, and the histograms on the right side show the normalized probability distribution of area equivalent diameters of all recorded ice crystals for that bin. To avoid uncertainties at the lower detection limit of the CIP, only images of particles with an equivalent diameter larger than 30 µm are considered and out-of-focus images are rejected.

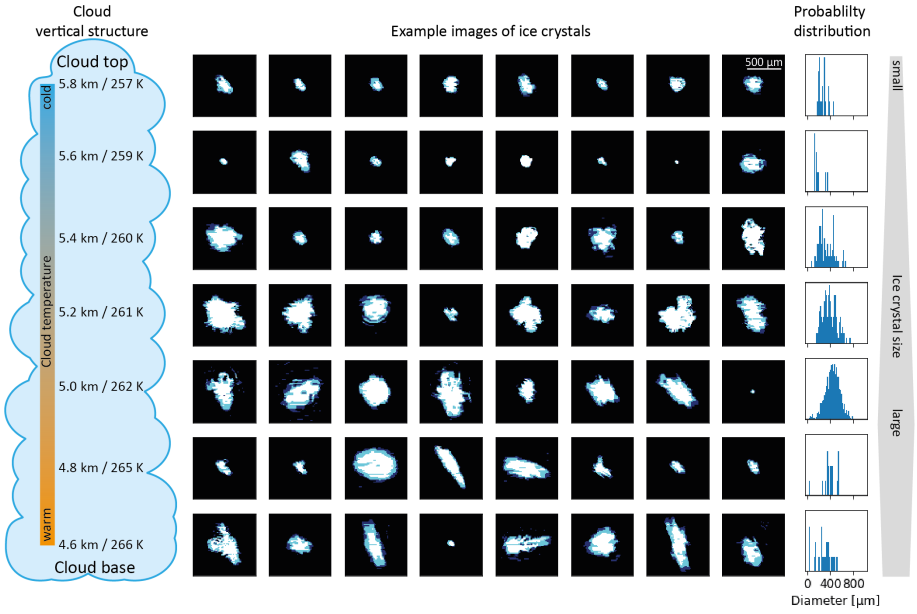

Figure 7. Vertical structure of the cloud embedded in a dust layer sampled between 15:40 and 15:50. The sketch on the left side illustrates each altitude bin with a corresponding average temperature. Each row of images shows examples of ice crystals at the corresponding altitude bin. Normalized probability distributions present the area equivalent diameters of imaged particles within the corresponding altitude bin. Only images of ice crystals larger than 30 µm are considered and out-of-focus images are rejected.

Particle images and probability distributions of equivalent diameter indicate that the ice crystals in the upper part of the cloud (5.6 and 5.8 km) are smaller (248 ± 98 µm) compared to 428 ± 130 µm in the middle part of the cloud (5.0 to 5.4 km). In the lowest layer of the cloud (4.6 and 4.8 km), the sizes of the ice crystals decrease relative to the middle part of the cloud slightly to 347 ± 129 µm.

3.3 CCN activation and growth of mineral dust particles into small liquid cloud droplets

Figure 8 represents a magnified view of Figure 4 focusing on the time intervals between 15:04:40 and 15:05:30 and between 16:19:04 and 16:19:50 (red and blue rectangles). During these periods, significant changes in the particle number size distributions – particularly in the size range below approx. 40 to 50 µm are visible. The count median diameter (CMD) calculated for the CAS measurements (black-dotted line in panel d) demonstrates the change in the size distribution very clearly.

https://doi.org/10.5194/egusphere-2026-531
Preprint. Discussion started: 2 April 2026

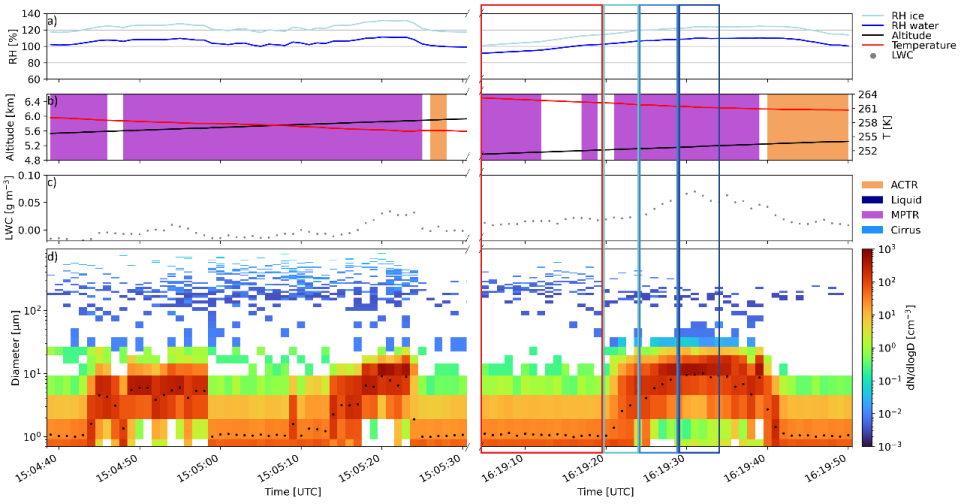

Figure 8. Magnified view of Figure 4 focusing on two time periods: 15:04:40 – 15:05:30 and 16:19:04 – 16:19:50. The black dotted line in panel d) represents the count median diameter (CMD) for the size distribution measured with the CAS. Colored boxes represent different stages of the growth event between 16:19:04 – 16:19:50 used for the size distributions in Figure 9. Note: The x-axis is discontinuous at 15:05:30.

Three CCN activation events (15:04:40 – 15:05:00, 15:05:10 – 15:05:25, and 16:19:04 – 16:19:50), with an increase of CMD from approx. 1 µm to values around 10 µm, are visible. During these periods, the particle number concentrations peak at approx. 10 µm with dN/dlogD between 10^2 and 10^3 cm^{-3}. Furthermore, significantly lower concentrations are observed in the size range around 1 µm compared to the size distributions during periods before and after the events. All three activation events are accompanied by increasing relative humidity values, with RH_w values ranging from around 100% to supersaturated conditions. Average temperatures during the three events are 258, 256, and 261 K.

To analyze the particle growth in more detail, size distribution measurements from the CAS were processed with the size distribution retrieval presented in section 2.2.3. Figure 9 illustrates the results for the last activation case (16:19:04 - 16:19:50). The three dotted lines in different shades of blue represent the size distributions at different stages during the particle activation and growth event, which correspond to the colored boxes in Figure 8. The red dots represent the size distribution measured preceding the activation event also corresponding to the time period in the red box in Figure 8. The blue curves are from the different stages during the growth process, with the increasing darkness of blue indicating a more advanced growth. The continuous red line represents the size distribution of the same mineral dust layer measured outside of clouds between 14:46 and 14:53 (see Figure 4). The blue shaded area below the dark blue curve in Figure 9 represents the particle number concentration in the final observed growth stage, which we define as the small cloud droplet number concentration ($N_{droplet}$), i.e., 88.7 cm^{-3}. The red shaded area shows the cumulative aerosol particle number concentration obtained by integrating the mineral dust layer size distribution from the largest towards smaller sizes, stopping when the cumulative number concentration equals $N_{droplet}$, i.e. the number concentration of activated and grown particles. The left end of this red-shaded area defines the maximum activation diameter ($D_{act,\,max}$), which is 0.29 µm for the presented case. The 50% activation diameter ($D_{act,\,50}$) represents the case that only 50% of all particles in each size class in the dust layer start to grow (red shaded area with dots) and is therefore smaller (0.17 µm) than $D_{act,\,max}$.

https://doi.org/10.5194/egusphere-2026-531
Preprint. Discussion started: 2 April 2026

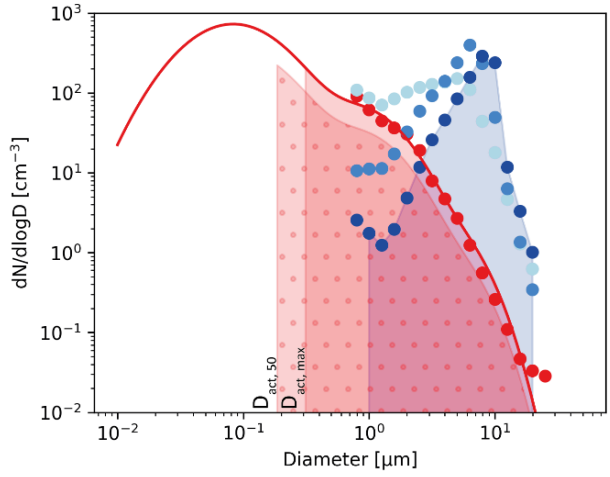

Figure 9. Particle number size distribution for the particle activation and growth event (16:19:04 – 16:19:50). The blue dots represent the size distributions at different stages during the particle growth (increasing darkness of blue indicating more advanced growth) and correspond to the same colored boxes in Figure 8. The blue shaded area below the dark blue dotted curve represents the total number of small droplets which had grown during the CCN activation event. The red line represents the complete size distribution of the mineral dust layer. Maximum activation diameter ($D_{act, max}$) and 50% activation diameter ($D_{act, 50}$) are indicated by the left ends of the red shaded area and red shaded area with dots, respectively.

Table 2. Number concentration of small cloud droplets ($N_{droplet}$) and corresponding maximum activation diameter ($D_{act, max}$), 50% activation diameter ($D_{act, 50}$), and liquid water content (LWC) calculated from the size distribution for particles larger than 1 µm for all three events. The calculations are restricted to the measurements from the CAS instrument and values are calculated for STP conditions.

Event Time [UTC]	$N_{droplet}$ [cm^{-3}]	$D_{act, max}$ [µm]	$D_{act, 50}$ [µm]	LWC_{SD} [g m^{-3}]
15:04	121.2	0.22	0.13	0.01
15:05	149.2	0.19	0.11	0.02
16:19	88.7	0.29	0.17	0.03
Average	119.7	0.23	0.14	0.02

The results from the calculations for all three events are summarized in Table 2. The average of the small cloud droplet number concentration is 119.7cm^{-3}. Average values for $D_{act, 50}$ and $D_{act, max}$ are 0.14 µm and 0.23 µm, respectively.

In addition to the in-situ measurements, DWL observations are used to retrieve information about the three-dimensional wind and the location of aerosol layers and clouds in the vertical column below the aircraft. Figure 10 presents the uncalibrated backscatter signal (panel a) and the vertical wind (panel b) for the first vertical profile (approx. 15:00 to 15:20) of the time series presented in Figure 4.

https://doi.org/10.5194/egusphere-2026-531
Preprint. Discussion started: 2 April 2026

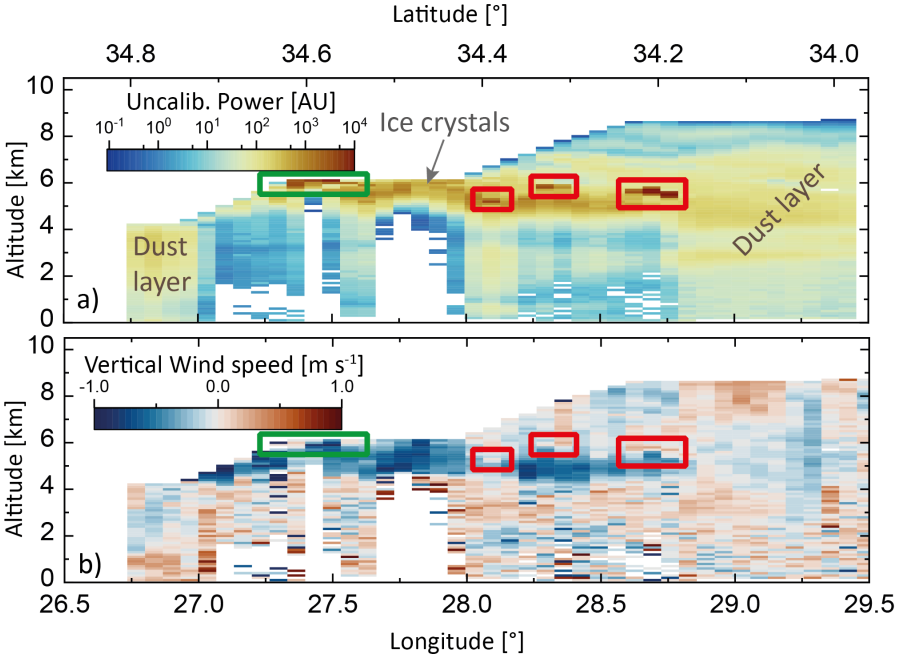

Figure 10. a) Uncalibrated backscatter and b) vertical wind speed from the DLR Doppler wind lidar (DWL) measured during the vertical profile between approx. 15:00 and 15:20. Panel a) indicates the dust layer and the ice crystal-containing clouds with labels in grey text. The green and red boxes in a) and b) mark the locations of CCN activation events.

The uncalibrated backscatter in panel a) visualizes the mineral dust layer with elevated signals of measured power around 10^2 AU at latitudes between 26.75° and 27.0° and 28.75° and 29.5° (red-marked area in Figure 3). Between 28.75° and 29.5° (Figure 10), the mineral dust layer extends from near the surface to altitudes near 8km, with the most intense lidar signal between 4 and 5km altitude. At latitudes between 27.25° and 28.75°, the uncalibrated backscatter signal shows a layer of elevated power with values around 10^3 AU between 5 and 6 km. This time period also contains the clouds visible in the in situ measurements shown in Figure 4. The green and red boxes in Figure 10 highlight locations of very high (10^4) backscatter signals. For the green box, both lidar observations and in situ sampling data are available. This corresponds to the CCN activation and growth event between 15:04:40 – 15:05:30 (see Figure 8). Figure 10b presents the vertical wind velocity, with blue and red represent descending and ascending motion, respectively, and also shows the locations of the green and red boxes. Compared to the cloud layer between 5 and 6 km, which in general exhibits a descending motion, the airmasses of the green and red boxes indicate a positive vertical wind speed, i.e. updrafts.

4 Discussion

Two different processes of aerosol-cloud interactions have been observed within the dust-embedded cloud on 20 April 2017. This section will examine these two processes in detail. Section 4.1 evaluates the hypothesis that heterogeneous ice nucleation of mineral dust particles formed the ice crystals at the cloud top already at temperatures around 257K, and compares the observations with results from laboratory experiments and

https://doi.org/10.5194/egusphere-2026-531
Preprint. Discussion started: 2 April 2026

commonly used parameterizations. Section 4.2 examines the activation of mineral dust particles into small liquid droplets and compares the findings from this study to a laboratory experiment.

4.1 Heterogeneous ice nucleation of mineral dust particles

In the previous section, ice crystals with sizes between approx. 30 and 930 µm were observed in a cloud embedded in a mineral dust layer. Figure 6 and Figure 7 revealed the cloud top as to be the location of the smallest ice crystals. Assuming that this is also the formation location of these ice crystals and no significant processes other than the growth of the ice crystals happened since the formation, we formulate the hypothesis that heterogeneous ice nucleation on super- micron mineral dust particles formed these ice crystals.

The mineral dust layer, extending from near the ground to altitudes above the cloud top, provides a significant reservoir of super-micron mineral dust particles ($N_{dust,\ D>1\mu m,\ STP}$ = 17.52 cm^{-3}). At the cloud top (5.8 km), the RH_i conditions were supersaturated with an average RH_i of 105.9 % (±1.0 %). Based on results of laboratory studies from Kanji and Abbatt (2006), the observed RH_i is within the range of ice onset relative humidity of super-micron Saharan dust (102 - 108 %) for deposition freezing. Hence, these findings suggest favorable conditions for the ice particle nucleation on the mineral dust, potentially due to deposition freezing. A common metric to compare the ice nucleation ability of different aerosols is the ice-active surface site density n_s. Following the description for polydisperse aerosol in Kanji et al. (2017) $n_s = N_{ice}/A_{total}$ where N_{ice} is the number of ice crystals in cm^{-3} and A_{total} is the surface area of the aerosol size distribution in cm^2 cm^{-3}. The average number concentration of ice crystals larger than 30 µm are $N_{D>30\mu m}$ = 0.0010 ± 0.0005 cm^{-3} and $N_{D>30\mu m,\ STP}$ = 0.0019 ± 0.0009 cm^{-3} at STP conditions. Since the measurements of the ice crystals and the mineral dust layer were performed at different pressure and temperature conditions, the $N_{D>30\mu m,\ STP}$ is utilized for the N_{ice} term. For A_{total}, only the super-micron aerosol of the investigated mineral dust layer is considered. A_{total} at STP conditions is 2.67x10^{-6} cm^2 cm^{-3} and results in an average n_s = 699 ± 348 cm^{-2}. This value is in good agreement with reported values for K-feldspar summarized in Kanji et al. (2017), which also agrees with the contribution of feldspar to the chemical composition of the sampled mineral dust layer (see Figure 5). Niemand et al. (2012) and Atkinson et al. (2013) provide temperature-dependent parameterizations of n_s for mineral dust based on the results from laboratory measurements. The applications of the two parameterizations in the cloud top region results in $n_{s,\ Niemand}$ = 2899 ± 392 cm^{-2} and $n_{s,\ Atkinson}$ = 4014 ± 1081 cm^{-2}. Both parametrizations are in good agreement with n_s calculated from the measured ice crystal concentration, especially when considering that the entire range of possible n_s values spans over 12 magnitudes. The comparison of predicted INP concentrations from two commonly used parameterizations for general aerosol (D10) and dust aerosol (D15) with the observed $N_{D>30\mu m}$ was shown in panel b) of Figure 6. In the cloud top region at 5.8 km, the average predicted INPs and $N_{D>30\mu m}$ agree by a factor of 0.67 and 0.43 for D10 and D15, respectively, which we consider an adequate consistency.

Comparisons of the ice-active surface site density n_s and commonly used INP parametrizations D10 and D15 with the observed ice crystal concentration $N_{D>30\mu m}$, show good agreement. However, for all comparisons, $N_{D>30\mu m}$ slightly underestimates the parameterizations. The sedimentation of ice crystals may have an effect, since ice crystals with a diameter of 100 µm are approximated to fall with 0.1 m s^{-1} with increased velocity for larger ice crystals (Gasparini et al., 2017; Spichtinger and Gierens, 2009). Figure 10 provides evidence for the sedimentation of the ice crystals. Panel a) shows the cloud layer with ice crystals in a light red color with an uncalibrated power of approx. 10^3 AU and a grey label “Ice crystals”. The corresponding area in panel b) shows negative vertical velocity in blue, which indicates a falling motion of the particles. Consequently, between the formation of the ice

https://doi.org/10.5194/egusphere-2026-531
Preprint. Discussion started: 2 April 2026

crystals and the measurements of $N_{D<30\mu m}$, some ice crystals have already fallen into lower altitude layers and, therefore, $N_{D<30\mu m}$ does not completely reflect all ice crystals nucleated from the mineral dust particles. Nevertheless, the comparison of the ice crystal measurements at the cloud top with parameterizations and laboratory results of ice onset relative humidity and INP strengthens the hypothesis that the super-micron mineral dust particles acted as INPs, which nucleated potentially via deposition mode freezing to the observed ice crystals.

4.2 Mineral dust as CCN

Sudden particle activation and growth events of a large number of aerosol particles to sizes in the range around 10 µm were observed in the time periods between 15:04:40 and 15:05:30 and between 16:19:04 and 16:19:50 (see Figure 8). The change of the particle size distribution during these events is depicted in Figure 9 and revealed an average number concentration of newly formed droplets of 119.7 cm^{-3} (Table 2). The presence of droplets is indicated with measurements of the CAPS hotwire LWC-sensor, showing an increased LWC_{hot} during the three CCN activation and growth events (see Figure 8 panel c). The first event at 15:04 shows only a minor increase to a maximum LWC of 0.009 g m^{-3}. For the second (15:05) and third (16:19) events, a more significant increase with a maximum LWC_{hot} of 0.034 g m^{-3} and 0.070 g m^{-3}, respectively, were measured. A comparison of the maximum LWC_{hot} value with the LWC_{SD} values calculated from the CAS size distributions for all particles larger than 1µm (Table 2) reveals larger values for the hotwire measurements. However, because the hotwire sensor also measures about 10-20% of the ice crystal mass, the agreement of LWC_{hot} and LWC_{SD} confirms that the particles at 10 µm are small droplets. The three CCN activation and growth events show that the aerosol particles in the mineral dust layer act as cloud condensation nuclei forming the small droplets. The integration of the mineral dust layer size distribution starting from the largest to smaller sizes obtained an average activation diameter between $D_{act,\ 50}$ = 0.14 µm and $D_{act,\ max}$ = 0.23 µm. This range of potential activation diameters is in excellent agreement with laboratory studies, which found the activation of Saharan mineral dust particles larger than approx. 0.2 µm already at low (0.2-0.3%) supersaturation (Herich et al., 2009; Koehler et al., 2009). A rough approximation of the RH_w values for the start of the observed CCN activation can be seen in Figure 11, which depicts the count median diameter (CMD) as a function of the RH_w for the three CCN activation events at 15:04 (blue), 15:05 (orange) and 16:19 (green). CMD values start to increase at RH_w between 102 and 104% and continue to increase to approx. 10 µm with increasing RH_w. These RH_w values, corresponding to a supersaturation between 2 and 4%, are higher than the results from the laboratory studies. However, it is likely that mineral dust particles sporadically activate at lower supersaturations but the temporal and instrumental resolution of the airborne instrumentation of this study does not allow such a precise investigation. The largest RH_w values of the three events are at 111% (see Figure 11).

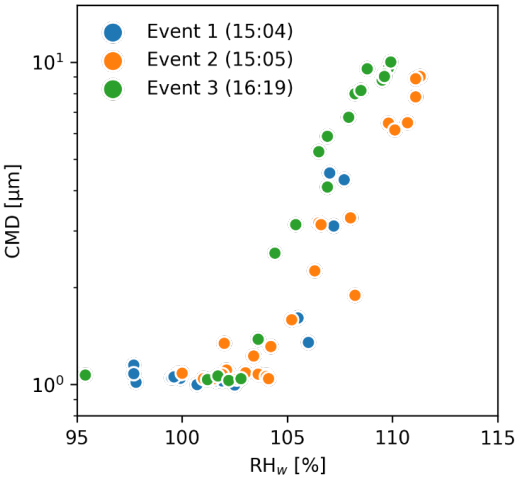

Figure 11. Count median diameter (CMD) as a function of RH_w for the three CCN activation events at 15:04 (blue), 15:05 (orange) and 16:19 (green) presented in Figure 9.

https://doi.org/10.5194/egusphere-2026-531
Preprint. Discussion started: 2 April 2026

Such high supersaturations can occur when saturated airmasses are lifted since adiabatic cooling decreases the saturation pressure with respect to water and, hence, increases the relative humidity (Wallace and Hobbs, 2006). The observed high-supersaturation values during the CCN activation events lead to the second hypothesis of this study, namely, that sudden small-scale vertical lifting events initiated the observed CCN activation.

Measurements from DWL can be utilized to investigate the vertical motion of the airmasses. Figure 10a indicates the region of the first (15:04) and second (15:05) CCN activation event with a green box where the uncalibrated power shows an intense signal. More of such intense signal events in the DWL measurements are visible within the dust-embedded clouds – highlighted in red boxes. Like the observed CCN activation events, these events occur at comparable altitudes inside the mineral dust layer. Hence, we conclude that they are also events of CCN activation. All of these potential CCN activation events are connected to vertical lifting, which can be seen by the positive vertical wind speed in the green and red boxes in panel b).

Bringing together the findings from the DWL measurements and the three analyzed CCN activation events, there is evidence to support the hypothesis that small-scale adiabatic lifting events are responsible for the CCN activation of mineral dust particles into supercooled liquid droplets with a mode diameter of approximately 10 µm. The lower limit of activation diameter is approximated to be between 0.14 and 0.23 µm, which is in very good agreement with laboratory experiments. Some of these newly formed liquid droplets may also turn into ice crystals if freezing is initiated through, e.g., immersion or contact freezing.

5 Summary

During the A-LIFE field campaign, unique measurements of clouds embedded in an intense Saharan mineral dust plume were conducted in the Eastern Mediterranean on 20 April 2017. In situ measurements of meteorological parameters and liquid water content (LWC), aerosol and cloud particle size distributions, and airborne Doppler wind lidar (DWL) observations were utilized to investigate these clouds concerning the CCN and INP properties of mineral dust. The aerosol and cloud particle size distributions were obtained from the CAS optical spectrometer of the Cloud, Aerosol, and Precipitation Spectrometer (CAPS) and processed with the novel UNIVIE size distribution retrieval introduced in this study. Considering instrumental uncertainties, this algorithm reports particle sizes in geometric diameters taking non-sphericity and refractive indices of the measured aerosol into account. LWC measurements from the hotwire sensor of CAPS were calibrated with a new method utilizing a machine-learning-based method presented in this manuscript. These new algorithms enabled a detailed analysis of clouds -embedded in the Saharan mineral dust layer, uncovering two distinct aerosol-cloud interactions processes:

- Ice nucleating particle (INP) closure reveals that mineral dust particles served as ice nuclei for the ice crystals observed in the dust-embedded cloud, most likely via deposition mode freezing.
- Mineral dust particles were activated as CCN and grew into small liquid droplets during CCN activation events triggered by water supersaturated conditions caused by vertical lifting processes.

For the INP closure, cloud-top ice crystal number concentrations and the particle size distribution of the mineral dust layer were used to determine the role of the mineral dust in the ice crystal formation of the observed dust-embedded cloud. The ice crystal number concentration was considered as a surrogate for the INP concentration during the nucleation of the ice crystals. Comparisons of cloud top relative humidity with ice onset relative humidity measurements from laboratory experiments revealed an overlapping agreement and confirmed deposition

https://doi.org/10.5194/egusphere-2026-531
Preprint. Discussion started: 2 April 2026

mode freezing as the potential nucleation mechanism. Commonly used INP parameterizations were applied to the size distribution of the mineral dust layer and exhibited a slight overestimation when compared to the cloud top ice crystal concentration. However, sedimentation effects – moving larger ice crystals into lower levels of the cloud – may explain this overestimation.

For the second aerosol-cloud interaction process, we analyzed particle number size distributions and LWC observations from three CCN activation events. These confirm that mineral dust activated as CCN and grew into liquid droplets with a modal diameter of approx. 10 µm. The calculated activation diameter of the mineral dust particles (i.e., the smallest particle diameter that can act as a nucleus for the growth of a liquid droplet) was between 0.13 and 0.23 µm, providing excellent agreement with laboratory studies. Doppler wind lidar (DWL) observations identified small-scale vertical lifting as the driver for pronounced water vapor supersaturation, creating conditions for CCN activation of the mineral dust particles. Some of these small droplets may have subsequently frozen, also contributing to the observed ice crystal number concentration.

6 Author contributions

M. Dollner: Conceptualization, Writing – original draft, review & editing, Investigation, Methodology, Software, Formal analysis, Data curation, Validation, Visualization. **J. Gasteiger:** Investigation, Data curation. **K. Kandler:** Investigation, Data curation. **M. Schöberl:** Investigation, Data curation, Validation. **S. Aryasree:** Investigation, Data curation. **B. Witschas:** Investigation, Data curation. **B. Weinzierl:** Conceptualization, Writing – review & editing, Supervision, Investigation, Resources, Project administration. All authors commented on previous versions of the manuscript. All authors read and approved the final manuscript.

7 Data availability

The data of this study will be made publicly available in the data archive Phaidra of the University of Vienna under the DOI: 10.25365/phaidra.791.

8 Competing interests

The contact authors have declared that none of the authors have any competing interests.

References

Adebiyi, A., Kok, J. F., Murray, B. J., Ryder, C. L., Stuut, J.-B. W., Kahn, R. A., Knippertz, P., Formenti, P., Mahowald, N. M., Pérez García-Pando, C., Klose, M., Ansmann, A., Samset, B. H., Ito, A., Balkanski, Y., Di Biagio, C., Romanias, M. N., Huang, Y., and Meng, J.: A review of coarse mineral dust in the Earth system, Aeolian Research, 60, 100849, https://doi.org/10.1016/j.aeolia.2022.100849, 2023.

Adebiyi, A. A. and Kok, J. F.: Climate models miss most of the coarse dust in the atmosphere, Sci. Adv., 6, eaaz9507, https://doi.org/10.1126/sciadv.aaz9507, 2020.

Aryasree, S., Kandler, K., Benker, N., Walser, A., Tipka, A., Dollner, M., Seibert, P., and Weinzierl, B.: Vertical Variability in morphology, chemistry and optical properties of the transported Saharan air layer measured from Cape Verde and the Caribbean, Royal Society Open Science, 11, 231433, https://doi.org/10.1098/rsos.231433, 2024.

https://doi.org/10.5194/egusphere-2026-531
Preprint. Discussion started: 2 April 2026

Atkinson, J. D., Murray, B. J., Woodhouse, M. T., Whale, T. F., Baustian, K. J., Carslaw, K. S., Dobbie, S., O'Sullivan, D., and Malkin, T. L.: The importance of feldspar for ice nucleation by mineral dust in mixed-phase clouds, Nature, 498, 355–358, https://doi.org/10.1038/nature12278, 2013.

Baumgardner, D., Abel, S. J., Axisa, D., Cotton, R., Crosier, J., Field, P., Gurganus, C., Heymsfield, A., Korolev, A., Krämer, M., Lawson, P., McFarquhar, G., Ulanowski, Z., and Um, J.: Cloud Ice Properties: In Situ Measurement Challenges, Meteorological Monographs, 58, 9.1-9.23, https://doi.org/10.1175/amsmonographs-d-16-0011.1, 2017.

Bond, T. C. and Bergstrom, R. W.: Light Absorption by Carbonaceous Particles: An Investigative Review, Aerosol Science and Technology, 40, 27–67, https://doi.org/10.1080/02786820500421521, 2006.

Brock, C. A., Wagner, N. L., Anderson, B. E., Attwood, A. R., Beyersdorf, A., Campuzano-Jost, P., Carlton, A. G., Day, D. A., Diskin, G. S., Gordon, T. D., Jimenez, J. L., Lack, D. A., Liao, J., Markovic, M. Z., Middlebrook, A. M., Ng, N. L., Perring, A. E., Richardson, M. S., Schwarz, J. P., Washenfelder, R. A., Welti, A., Xu, L., Ziemba, L. D., and Murphy, D. M.: Aerosol optical properties in the southeastern United States in summer – Part 1: Hygroscopic growth, Atmos. Chem. Phys., 16, 4987–5007, https://doi.org/10.5194/acp-16-4987-2016, 2016.

Brock, C. A., Froyd, K. D., Dollner, M., Williamson, C. J., Schill, G., Murphy, D. M., Wagner, N. J., Kupc, A., Jimenez, J. L., Campuzano-Jost, P., Nault, B. A., Schroder, J. C., Day, D. A., Price, D. J., Weinzierl, B., Schwarz, J. P., Katich, J. M., Wang, S., Zeng, L., Weber, R., Dibb, J., Scheuer, E., Diskin, G. S., DiGangi, J. P., Bui, T., Dean-Day, J. M., Thompson, C. R., Peischl, J., Ryerson, T. B., Bourgeois, I., Daube, B. C., Commane, R., and Wofsy, S. C.: Ambient aerosol properties in the remote atmosphere from global-scale in situ measurements, Atmos. Chem. Phys., 21, 15023–15063, https://doi.org/10.5194/acp-21-15023-2021, 2021.

Chouza, F., Reitebuch, O., Groß, S., Rahm, S., Freudenthaler, V., Toledano, C., and Weinzierl, B.: Retrieval of aerosol backscatter and extinction from airborne coherent Doppler wind lidar measurements, Atmospheric Measurement Techniques, 8, 2909–2926, https://doi.org/10.5194/amt-8-2909-2015, 2015.

Chouza, F., Reitebuch, O., Jähn, M., Rahm, S., and Weinzierl, B.: Vertical wind retrieved by airborne lidar and analysis of island induced gravity waves in combination with numerical models and in situ particle measurements, Atmos. Chem. Phys., 16, 4675–4692, https://doi.org/10.5194/acp-16-4675-2016, 2016.

Chouza, F., Witschas, B., and Reitebuch, O.: Heterodyne high-spectral-resolution lidar, Appl. Opt., 56, 8121, https://doi.org/10.1364/AO.56.008121, 2017.

Cober, S. G., Isaac, G. A., Korolev, A. V., and Strapp, J. W.: Assessing cloud-phase conditions, J. Appl. Meteorol., 40, 1967–1983, https://doi.org/10.1175/1520-0450(2001)040%253C1967:acpc%253E2.0.co;2, 2001.

Cziczo, D. J., Froyd, K. D., Hoose, C., Jensen, E. J., Diao, M. H., Zondlo, M. A., Smith, J. B., Twohy, C. H., and Murphy, D. M.: Clarifying the Dominant Sources and Mechanisms of Cirrus Cloud Formation, Science, 340, 1320–1324, https://doi.org/10.1126/science.1234145, 2013.

Cziczo, D. J., Ladino, L., Boose, Y., Kanji, Z. A., Kupiszewski, P., Lance, S., Mertes, S., and Wex, H.: Measurements of Ice Nucleating Particles and Ice Residuals, Meteorological Monographs, 58, 8.1-8.13, https://doi.org/10.1175/amsmonographs-d-16-0008.1, 2017.

DeMott, P. J., Prenni, A. J., Liu, X., Kreidenweis, S. M., Petters, M. D., Twohy, C. H., Richardson, M. S., Eidhammer, T., and Rogers, D. C.: Predicting global atmospheric ice nuclei distributions and their impacts on climate, PNAS, 107, 11217–11222, https://doi.org/10.1073/pnas.0910818107, 2010.

DeMott, P. J., Prenni, A. J., McMeeking, G. R., Sullivan, R. C., Petters, M. D., Tobo, Y., Niemand, M., Möhler, O., Snider, J. R., Wang, Z., and Kreidenweis, S. M.: Integrating laboratory and field data to quantify the immersion freezing ice nucleation activity of mineral dust particles, Atmos. Chem. Phys., 15, 393–409, https://doi.org/10.5194/acp-15-393-2015, 2015.

Dollner, M., Gasteiger, J., Schöberl, M., Gattringer, A., Beres, N. D., Bui, T. P., Diskin, G., and Weinzierl, B.: The *Cloud Indicator*: A novel algorithm for automatic detection and classification of clouds using airborne in situ observations, Atmospheric Research, 107504, https://doi.org/10.1016/j.atmosres.2024.107504, 2024.

https://doi.org/10.5194/egusphere-2026-531
Preprint. Discussion started: 2 April 2026

Eidhammer, T., DeMott, P. J., Prenni, A. J., Petters, M. D., Twohy, C. H., Rogers, D. C., Stith, J., Heymsfield, A., Wang, Z., Pratt, K. A., Prather, K. A., Murphy, S. M., Seinfeld, J. H., Subramanian, R., and Kreidenweis, S. M.: Ice Initiation by Aerosol Particles: Measured and Predicted Ice Nuclei Concentrations versus Measured Ice Crystal Concentrations in an Orographic Wave Cloud, Journal of the Atmospheric Sciences, 67, 2417–2436, https://doi.org/10.1175/2010JAS3266.1, 2010.

Field, P. R., Hogan, R. J., Brown, P. R. A., Illingworth, A. J., Choularton, T. W., Kaye, P. H., Hirst, E., and Greenaway, R.: Simultaneous radar and aircraft observations of mixed-phase cloud at the 100 m scale, Q. J. R. Meteorol. Soc., 130, 1877–1904, https://doi.org/10.1256/qj.03.102, 2004.

Froyd, K. D., Murphy, D. M., Brock, C. A., Campuzano-Jost, P., Dibb, J. E., Jimenez, J.-L., Kupc, A., Middlebrook, A. M., Schill, G. P., Thornhill, K. L., Williamson, C. J., Wilson, J. C., and Ziemba, L. D.: A new method to quantify mineral dust and other aerosol species from aircraft platforms using single-particle mass spectrometry, Atmospheric Measurement Techniques, 12, 6209–6239, https://doi.org/10.5194/amt-12-6209-2019, 2019.

Froyd, K. D., Yu, P., Schill, G. P., Brock, C. A., Kupc, A., Williamson, C. J., Jensen, E. J., Ray, E., Rosenlof, K. H., Bian, H., Darmenov, A. S., Colarco, P. R., Diskin, G. S., Bui, T., and Murphy, D. M.: Dominant role of mineral dust in cirrus cloud formation revealed by global-scale measurements, Nat. Geosci., 1–7, https://doi.org/10.1038/s41561-022-00901-w, 2022.

Gasparini, B., Münch, S., Poncet, L., Feldmann, M., and Lohmann, U.: Is increasing ice crystal sedimentation velocity in geoengineering simulations a good proxy for cirrus cloud seeding?, Atmos. Chem. Phys., 17, 4871–4885, https://doi.org/10.5194/acp-17-4871-2017, 2017.

Groß, S., Freudenthaler, V., Haarig, M., Ansmann, A., Toledano, C., Mateos, D., Seibert, P., Mamouri, R.-E., Nisantzi, A., Gasteiger, J., Dollner, M., Tipka, A., Schöberl, M., Teri, M., and Weinzierl, B.: Characterization of aerosol over the eastern Mediterranean by polarization-sensitive Raman lidar measurements during A-LIFE – aerosol type classification and type separation, Atmospheric Chemistry and Physics, 25, 3191–3211, https://doi.org/10.5194/acp-25-3191-2025, 2025.

Herich, H., Tritscher, T., Wiacek, A., Gysel, M., Weingartner, E., Lohmann, U., Baltensperger, U., and Cziczo, D. J.: Water uptake of clay and desert dust aerosol particles at sub- and supersaturated water vapor conditions, Phys. Chem. Chem. Phys., 11, 7804–7809, https://doi.org/10.1039/B901585J, 2009.

Hoose, C. and Möhler, O.: Heterogeneous ice nucleation on atmospheric aerosols: a review of results from laboratory experiments, Atmospheric Chemistry and Physics, 12, 9817–9854, https://doi.org/10.5194/acp-12-9817-2012, 2012.

Huneeus, N., Schulz, M., Balkanski, Y., Griesfeller, J., Prospero, J., Kinne, S., Bauer, S., Boucher, O., Chin, M., Dentener, F., Diehl, T., Easter, R., Fillmore, D., Ghan, S., Ginoux, P., Grini, A., Horowitz, L., Koch, D., Krol, M. C., Landing, W., Liu, X., Mahowald, N., Miller, R., Morcrette, J.-J., Myhre, G., Penner, J., Perlwitz, J., Stier, P., Takemura, T., and Zender, C. S.: Global dust model intercomparison in AeroCom phase I, Atmospheric Chemistry and Physics, 11, 7781–7816, https://doi.org/10.5194/acp-11-7781-2011, 2011.

Jensen, E. J., Kaercher, B., Ueyama, R., Pfister, L., Bui, T. V., Diskin, G. S., DiGangi, J. P., Woods, S., Lawson, R. P., Froyd, K. D., and Murphy, D. M.: Heterogeneous Ice Nucleation in the Tropical Tropopause Layer, J. Geophys. Res.-Atmos., 123, 12210–12227, https://doi.org/10.1029/2018JD028949, 2018.

Kandler, K., Lieke, K., Benker, N., Emmel, C., Küpper, M., Müller-Ebert, D., Ebert, M., Scheuvens, D., Schladitz, A., Schütz, L., and Weinbruch, S.: Electron microscopy of particles collected at Praia, Cape Verde, during the Saharan Mineral Dust Experiment: particle chemistry, shape, mixing state and complex refractive index, Tellus B: Chemical and Physical Meteorology, 63, 475–496, https://doi.org/10.1111/j.1600-0889.2011.00550.x, 2011.

Kanji, Z. A. and Abbatt, J. P. D.: Laboratory studies of ice formation via deposition mode nucleation onto mineral dust and n-hexane soot samples, Journal of Geophysical Research: Atmospheres, 111, https://doi.org/10.1029/2005JD006766, 2006.

Kanji, Z. A., Ladino, L. A., Wex, H., Boose, Y., Burkert-Kohn, M., Cziczo, D. J., and Krämer, M.: Overview of Ice Nucleating Particles, Meteorological Monographs, 58, 1.1-1.33, https://doi.org/10.1175/amsmonographs-d-16-0006.1, 2017.

https://doi.org/10.5194/egusphere-2026-531
Preprint. Discussion started: 2 April 2026

King, W. D., Parkin, D. A., and Handsworth, R. J.: A Hot-Wire Liquid Water Device Having Fully Calculable Response Characteristics, Journal of Applied Meteorology, 17, 1809–1813, https://doi.org/10.1175/1520-0450(1978)017%253C1809:ahwlwd%253E2.0.co;2, 1978.

Kinne, S., Schulz, M., Textor, C., Guibert, S., Balkanski, Y., Bauer, S. E., Berntsen, T., Berglen, T. F., Boucher, O., Chin, M., Collins, W., Dentener, F., Diehl, T., Easter, R., Feichter, J., Fillmore, D., Ghan, S., Ginoux, P., Gong, S., Grini, A., Hendricks, J., Herzog, M., Horowitz, L., Isaksen, I., Iversen, T., Kirkevåg, A., Kloster, S., Koch, D., Kristjansson, J. E., Krol, M., Lauer, A., Lamarque, J. F., Lesins, G., Liu, X., Lohmann, U., Montanaro, V., Myhre, G., Penner, J., Pitari, G., Reddy, S., Seland, O., Stier, P., Takemura, T., and Tie, X.: An AeroCom initial assessment – optical properties in aerosol component modules of global models, Atmospheric Chemistry and Physics, 6, 1815–1834, https://doi.org/10.5194/acp-6-1815-2006, 2006.

Koehler, K. A., Kreidenweis, S. M., DeMott, P. J., Petters, M. D., Prenni, A. J., and Carrico, C. M.: Hygroscopicity and cloud droplet activation of mineral dust aerosol, Geophysical Research Letters, 36, https://doi.org/10.1029/2009GL037348, 2009.

Kok, J. F., Ridley, D. A., Zhou, Q., Miller, R. L., Zhao, C., Heald, C. L., Ward, D. S., Albani, S., and Haustein, K.: Smaller desert dust cooling effect estimated from analysis of dust size and abundance, Nature Geosci, 10, 274–278, https://doi.org/10.1038/ngeo2912, 2017.

Korolev, A., McFarquhar, G., Field, P. R., Franklin, C., Lawson, P., Wang, Z., Williams, E., Abel, S. J., Axisa, D., Borrmann, S., Crosier, J., Fugal, J., Krämer, M., Lohmann, U., Schlenczek, O., Schnaiter, M., and Wendisch, M.: Mixed-Phase Clouds: Progress and Challenges, Meteorological Monographs, 58, 5.1-5.50, https://doi.org/10.1175/AMSMONOGRAPHS-D-17-0001.1, 2017.

Korolev, A. V., Strapp, J. W., Isaac, G. A., and Nevzorov, A. N.: The Nevzorov Airborne Hot-Wire LWC–TWC Probe: Principle of Operation and Performance Characteristics, Journal of Atmospheric and Oceanic Technology, 15, 1495–1510, https://doi.org/10.1175/1520-0426(1998)015%253C1495:TNAHWL%253E2.0.CO;2, 1998.

Mateos, D., Toledano, C., Calle, A., Román, R., Herreras-Giralda, M., González, R., Herrero-Anta, S., González-Fernández, D., Herrero-del Barrio, C., Nisantzi, A., Mamouri, R. E., Groß, S., Cachorro, V. E., de Frutos, Á. M., and Weinzierl, B.: Saharan and Arabian dust optical properties registered by sun photometry during A-LIFE field experiment in Cyprus, Atmospheric Chemistry and Physics, 26, 1993–2005, https://doi.org/10.5194/acp-26-1993-2026, 2026.

McFarquhar, G. M., Baumgardner, D., Bansemer, A., Abel, S. J., Crosier, J., French, J., Rosenberg, P., Korolev, A., Schwarzoenboeck, A., Leroy, D., Um, J., Wu, W., Heymsfield, A. J., Twohy, C., Detwiler, A., Field, P., Neumann, A., Cotton, R., Axisa, D., and Dong, J. Y.: Processing of Ice Cloud In Situ Data Collected by Bulk Water, Scattering, and Imaging Probes: Fundamentals, Uncertainties, and Efforts toward Consistency, in: Ice Formation and Evolution in Clouds and Precipitation: Measurement and Modeling Challenges, vol. 58, edited by: Baumgardner, D., McFarquhar, G. M., and Heymsfield, A. J., Amer Meteorological Society, Boston, https://doi.org/10.1175/amsmonographs-d-16-0007.1, 2017.

Metropolis, N. and Ulam, S.: The Monte Carlo Method, Journal of the American Statistical Association, 44, 335–341, https://doi.org/10.1080/01621459.1949.10483310, 1949.

Michel Flores, J., Bar-Or, R. Z., Bluvshtein, N., Abo-Riziq, A., Kostinski, A., Borrmann, S., Koren, I., Koren, I., and Rudich, Y.: Absorbing aerosols at high relative humidity: linking hygroscopic growth to optical properties, Atmospheric Chemistry and Physics, 12, 5511–5521, https://doi.org/10.5194/acp-12-5511-2012, 2012.

Moise, T., Flores, J. M., and Rudich, Y.: Optical Properties of Secondary Organic Aerosols and Their Changes by Chemical Processes, Chem. Rev., 115, 4400–4439, https://doi.org/10.1021/cr5005259, 2015.

Niemand, M., Möhler, O., Vogel, B., Vogel, H., Hoose, C., Connolly, P., Klein, H., Bingemer, H., DeMott, P., Skrotzki, J., and Leisner, T.: A Particle-Surface-Area-Based Parameterization of Immersion Freezing on Desert Dust Particles, Journal of the Atmospheric Sciences, 69, 3077–3092, https://doi.org/10.1175/JAS-D-11-0249.1, 2012.

Petters, M. D. and Kreidenweis, S. M.: A single parameter representation of hygroscopic growth and cloud condensation nucleus activity, Atmos. Chem. Phys., 7, 1961–1971, https://doi.org/10.5194/acp-7-1961-2007, 2007.

https://doi.org/10.5194/egusphere-2026-531
Preprint. Discussion started: 2 April 2026

Pisso, I., Sollum, E., Grythe, H., Kristiansen, N. I., Cassiani, M., Eckhardt, S., Arnold, D., Morton, D., Thompson, R. L., Groot Zwaaftink, C. D., Evangeliou, N., Sodemann, H., Haimberger, L., Henne, S., Brunner, D., Burkhart, J. F., Fouilloux, A., Brioude, J., Philipp, A., Seibert, P., and Stohl, A.: The Lagrangian particle dispersion model FLEXPART version 10.4, Geosci. Model Dev., 12, 4955–4997, https://doi.org/10.5194/gmd-12-4955-2019, 2019.

Ratcliffe, N. G., Ryder, C. L., Bellouin, N., Woodward, S., Jones, A., Johnson, B., Wieland, L.-M., Dollner, M., Gasteiger, J., and Weinzierl, B.: Long-range transport of coarse mineral dust: an evaluation of the Met Office Unified Model against aircraft observations, Atmospheric Chemistry and Physics, 24, 12161–12181, https://doi.org/10.5194/acp-24-12161-2024, 2024.

Rosenberg, P. D., Dean, A. R., Williams, P. I., Dorsey, J. R., Minikin, A., Pickering, M. A., and Petzold, A.: Particle sizing calibration with refractive index correction for light scattering optical particle counters and impacts upon PCASP and CDP data collected during the Fennec campaign, Atmospheric Measurement Techniques, 5, 1147–1163, https://doi.org/10.5194/amt-5-1147-2012, 2012.

Ryder, C. L., Highwood, E. J., Walser, A., Seibert, P., Philipp, A., and Weinzierl, B.: Coarse and giant particles are ubiquitous in Saharan dust export regions and are radiatively significant over the Sahara, Atmospheric Chemistry and Physics, 19, 15353–15376, https://doi.org/10.5194/acp-19-15353-2019, 2019.

Schöberl, M., Dollner, M., Gasteiger, J., Seibert, P., Tipka, A., and Weinzierl, B.: Characterization of the airborne aerosol inlet and transport system used during the A-LIFE aircraft field experiment, Atmospheric Measurement Techniques, 17, 2761–2776, https://doi.org/10.5194/amt-17-2761-2024, 2024.

Seibert, P. and Frank, A.: Source-receptor matrix calculation with a Lagrangian particle dispersion model in backward mode, Atmos. Chem. Phys., 4, 51–63, https://doi.org/10.5194/acp-4-51-2004, 2004.

Seinfeld, J. H. and Pandis, S. N.: Atmospheric chemistry and physics: from air pollution to climate change, 2nd ed., J. Wiley, Hoboken, N.J, 1203 pp., 2006.

Spanu, A., Dollner, M., Gasteiger, J., Bui, T. P., and Weinzierl, B.: Flow-induced errors in airborne in situ measurements of aerosols and clouds, Atmospheric Measurement Techniques, 13, 1963–1987, https://doi.org/10.5194/amt-13-1963-2020, 2020.

Spichtinger, P. and Gierens, K. M.: Modelling of cirrus clouds – Part 1a: Model description and validation, Atmos. Chem. Phys., 9, 685–706, https://doi.org/10.5194/acp-9-685-2009, 2009.

Stohl, A., Hittenberger, M., and Wotawa, G.: Validation of the lagrangian particle dispersion model FLEXPART against large-scale tracer experiment data, Atmospheric Environment, 32, 4245–4264, https://doi.org/10.1016/S1352-2310(98)00184-8, 1998.

Stohl, A., Forster, C., Frank, A., Seibert, P., and Wotawa, G.: Technical note: The Lagrangian particle dispersion model FLEXPART version 6.2, Atmos. Chem. Phys., 5, 2461–2474, https://doi.org/10.5194/acp-5-2461-2005, 2005.

Svenningsson, B., Rissler, J., Swietlicki, E., Mircea, M., Bilde, M., Facchini, M. C., Decesari, S., Fuzzi, S., Zhou, J., Mønster, J., and Rosenørn, T.: Hygroscopic growth and critical supersaturations for mixed aerosol particles of inorganic and organic compounds of atmospheric relevance, Atmos. Chem. Phys., 6, 1937–1952, https://doi.org/10.5194/acp-6-1937-2006, 2006.

Szymanski, W. W., Nagy, A., and Czitrovszky, A.: Optical particle spectrometry—Problems and prospects, Journal of Quantitative Spectroscopy and Radiative Transfer, 110, 918–929, https://doi.org/10.1016/j.jqsrt.2009.02.024, 2009.

Tang, I. N.: Chemical and size effects of hygroscopic aerosols on light scattering coefficients, J. Geophys. Res., 101, 19245–19250, https://doi.org/10.1029/96JD03003, 1996.

Tang, M., Cziczo, D. J., and Grassian, V. H.: Interactions of Water with Mineral Dust Aerosol: Water Adsorption, Hygroscopicity, Cloud Condensation, and Ice Nucleation, Chem. Rev., 116, 4205–4259, https://doi.org/10.1021/acs.chemrev.5b00529, 2016.

https://doi.org/10.5194/egusphere-2026-531
Preprint. Discussion started: 2 April 2026

Teri, M., Gasteiger, J., Heimerl, K., Dollner, M., Schöberl, M., Seibert, P., Tipka, A., Müller, T., Aryasree, S., Kandler, K., and Weinzierl, B.: Pollution affects Arabian and Saharan dust optical properties in the eastern Mediterranean, Atmospheric Chemistry and Physics, 25, 6633–6662, https://doi.org/10.5194/acp-25-6633-2025, 2025.

Tipka, A., Haimberger, L., and Seibert, P.: Flex_extract v7.1.2 – a software package to retrieve and prepare ECMWF data for use in FLEXPART, Geosci. Model Dev., 13, 5277–5310, https://doi.org/10.5194/gmd-13-5277-2020, 2020.

Vali, G., DeMott, P. J., Möhler, O., and Whale, T. F.: Technical Note: A proposal for ice nucleation terminology, Atmospheric Chemistry and Physics, 15, 10263–10270, https://doi.org/10.5194/acp-15-10263-2015, 2015.

Villanueva, D., Neubauer, D., Gasparini, B., Ickes, L., and Tegen, I.: Constraining the Impact of Dust-Driven Droplet Freezing on Climate Using Cloud-Top-Phase Observations, Geophysical Research Letters, 48, e2021GL092687, https://doi.org/10.1029/2021GL092687, 2021.

Wallace, J. M. and Hobbs, P. V.: Atmospheric science: an introductory survey, 2nd ed., Elsevier Academic Press, Amsterdam ; Boston, 483 pp., 2006.

Walser, A., Sauer, D., Spanu, A., Gasteiger, J., and Weinzierl, B.: On the parametrization of optical particle counter response including instrument-induced broadening of size spectra and a self-consistent evaluation of calibration measurements, Atmos. Meas. Tech., 10, 4341–4361, https://doi.org/10.5194/amt-10-4341-2017, 2017.

Weinzierl, B. and Coauthors: The A-LIFE field experiment in the Eastern Mediterranean: highlights from the airborne observations and insights into properties of absorbing aerosol mixtures, in prep.

Weinzierl, B., Petzold, A., Esselborn, M., Wirth, M., Rasp, K., Kandler, K., SchüTZ, L., Koepke, P., and Fiebig, M.: Airborne measurements of dust layer properties, particle size distribution and mixing state of Saharan dust during SAMUM 2006, Tellus B: Chemical and Physical Meteorology, 61, 96–117, https://doi.org/10.1111/j.1600-0889.2008.00392.x, 2009.

Weinzierl, B., Sauer, D., Esselborn, M., Petzold, A., Veira, A., Rose, M., Mund, S., Wirth, M., Ansmann, A., Tesche, M., Gross, S., and Freudenthaler, V.: Microphysical and optical properties of dust and tropical biomass burning aerosol layers in the Cape Verde region—an overview of the airborne in situ and lidar measurements during SAMUM-2, Tellus B: Chemical and Physical Meteorology, 63, 589–618, https://doi.org/10.1111/j.1600-0889.2011.00566.x, 2011.

Weinzierl, B., Ansmann, A., Prospero, J. M., Althausen, D., Benker, N., Chouza, F., Dollner, M., Farrell, D., Fomba, W. K., Freudenthaler, V., Gasteiger, J., Groß, S., Haarig, M., Heinold, B., Kandler, K., Kristensen, T. B., Mayol-Bracero, O. L., Müller, T., Reitebuch, O., Sauer, D., Schäfler, A., Schepanski, K., Spanu, A., Tegen, I., Toledano, C., and Walser, A.: The Saharan Aerosol Long-Range Transport and Aerosol–Cloud-Interaction Experiment: Overview and Selected Highlights, Bull. Amer. Meteor. Soc., 98, 1427–1451, https://doi.org/10.1175/BAMS-D-15-00142.1, 2017.

Witschas, B., Rahm, S., Dörnbrack, A., Wagner, J., and Rapp, M.: Airborne Wind Lidar Measurements of Vertical and Horizontal Winds for the Investigation of Orographically Induced Gravity Waves, Journal of Atmospheric and Oceanic Technology, 34, 1371–1386, https://doi.org/10.1175/JTECH-D-17-0021.1, 2017.

Witschas, B., Gisinger, S., Rahm, S., Dörnbrack, A., Fritts, D. C., and Rapp, M.: Airborne coherent wind lidar measurements of the momentum flux profile from orographically induced gravity waves, Atmospheric Measurement Techniques, 16, 1087–1101, https://doi.org/10.5194/amt-16-1087-2023, 2023.

Zieger, P., Fierz-Schmidhauser, R., Weingartner, E., and Baltensperger, U.: Effects of relative humidity on aerosol light scattering: results from different European sites, Atmos. Chem. Phys., 13, 10609–10631, https://doi.org/10.5194/acp-13-10609-2013, 2013.

Zieger, P., Väisänen, O., Corbin, J. C., Partridge, D. G., Bastelberger, S., Mousavi-Fard, M., Rosati, B., Gysel, M., Krieger, U. K., Leck, C., Nenes, A., Riipinen, I., Virtanen, A., and Salter, M. E.: Revising the hygroscopicity of inorganic sea salt particles, Nat Commun, 8, 15883, https://doi.org/10.1038/ncomms15883, 2017.